PCCP

ROYAL SOCIETY OF CHEMISTRY

PAPER

Published on 14 December 2020
Licensed under CC-BY 3.0

Check for updates

Cite this: *Phys. Chem. Chem. Phys.*, 2021, **23**, 1285

The effect of nanoparticulate PdO co-catalysts on the faradaic and light conversion efficiency of WO_3 photoanodes for water oxidation†

Anna A. Wilson,[a] Sacha Corby,[a] Laia Francàs,*[b] James R. Durrant[a] and Andreas Kafizas*[acd]

Received 25th November 2020,
Accepted 14th December 2020

DOI: 10.1039/d0cp06124g

rsc.li/pccp

WO_3 photoanodes offer rare stability in acidic media, but are limited by their selectivity for oxygen evolution over parasitic side reactions, when employed in photoelectrochemical (PEC) water splitting. Herein, this is remedied *via* the modification of nanostructured WO_3 photoanodes with surface decorated PdO as an oxygen evolution co-catalyst (OEC). The photoanodes and co-catalyst particles are grown using an up-scalable aerosol assisted chemical vapour deposition (AA-CVD) route, and their physical properties characterised by X-ray diffraction (XRD), Raman spectroscopy, X-ray photoelectron spectroscopy (XPS), scanning electron microscopy (SEM), high-resolution transmission electron microscopy (HR-TEM) and UV-vis absorption spectroscopy. Subsequent PEC and transient photocurrent (TPC) measurements showed that the use of a PdO co-catalyst dramatically increases the faradaic efficiency (FE) of water oxidation from 52% to 92%, whilst simultaneously enhancing the photocurrent generation and charge extraction rate. The Pd oxidation state was found to be critical in achieving these notable improvements to the photoanode performance, which is primarily attributed to the higher selectivity towards oxygen evolution when PdO is used as an OEC and the formation of a favourable junction between WO_3 and PdO, that drives band bending and charge separation.

1. Introduction

The conversion of solar energy into renewable fuels, whereby the energy is stored in chemical bonds, is an attractive approach to harvest solar energy whilst overcoming intermittency issues. Photoelectrochemical (PEC) water splitting achieves this in a single process, with the direct conversion and storage of solar energy in the chemical bonds of the hydrogen fuel produced.[1] Semiconductors are commonly employed as photoanodes for the water oxidation reaction, whereby light absorption initiates band gap excitation to yield photogenerated charges that can be utilised in the water splitting process. Under electrolyte conditions, the in-built electric field in the space charge layer of the semiconductor results in band bending that facilitates the separation and transport of photogenerated charges.[2]

Metal oxides have received extensive interest for PEC water splitting applications due to their low cost, high abundance, tunability and stability to photocorrosion.[2] Suitable electronic band structures for metal oxide photoanodes have a narrow band gap to maximise utilisation of the solar spectrum, and a valence band maximum (VBM) situated at a higher potential than that of water oxidation (+1.23 V_{RHE}). In addition to these constraints, high selectivity, efficient charge separation and sufficient charge carrier lifetimes are required for water oxidation to occur successfully. Due to the difficulties in achieving all of the aforementioned properties, a wide range of approaches have been examined to improve the design and synthesis of photoanode materials, including co-catalyst addition, heterojunction formation, doping, nanostructuring, and band gap engineering.[1,3]

WO_3 is a promising photoanode material for PEC water splitting.[4] With an indirect band gap of ~2.6–2.9 eV reported for monoclinic WO_3, between 6% and 10% of solar photons can be absorbed, compared to ~3% by anatase TiO_2 with a typical band gap of 3.2 eV.[2,3,5] Moreover, WO_3 exhibits rare stability for a metal oxide under acidic conditions and good charge transport properties. For example, WO_3 has a high electron

[a] *Department of Chemistry and Centre for Plastic Electronics, Imperial College London, White City Campus, London, W12 0BZ, UK. E-mail: a.kafizas@imperial.ac.uk*
[b] *Departament de Química, Universitat Autònoma de Barcelona, Cerdanyola del Vallès, Barcelona 08193, Spain. E-mail: laia.francas@uab.cat*
[c] *The Grantham Institute, Imperial College London, South Kensington, London, SW7 2AZ, UK*
[d] *London Centre for Nanotechnology, Imperial College London, SW7 2AZ, UK*
† Electronic supplementary information (ESI) available. See DOI: 10.1039/d0cp06124g

mobility ($\sim$12 cm^{-2} V^{-1} s^{-1})[5] compared to Fe_2O_3 (0.1 cm^{-2} V^{-1} s^{-1})[6] and TiO_2 (0.3 cm^{-2} V^{-1} s^{-1}).[5] However, in part due to the deep VBM of WO_3,[7] a multitude of species can be oxidised under irradiation, and thus side reactions can limit the efficiency of oxygen evolution through water oxidation.[8–10]

The addition of an oxygen evolution co-catalyst (OEC) can enhance performance by aiding charge separation, improving water oxidation kinetics and increasing reaction selectivity. Limited but encouraging results exist to date regarding the role of Pd species as OECs. Kim *et al.* studied the effect of a range of metal oxide OECs, in addition to FeOOH and Ag^+, on $BiVO_4$ photoanodes, and identified PdO_x as the best performing catalyst.[11] More recently, Joya *et al.* described nanoporous Pd as a benchmark electrocatalyst, with a low onset potential for electrocatalytic water oxidation (1.43 V_{RHE}) and high stability.[12]

In this work, nanoneedle WO_3 photoanodes are synthesised in a single-step *via* an up-scalable aerosol assisted chemical vapour deposition (AA-CVD) route and employed as photoanodes for PEC water oxidation.[13,14] With the aim of overcoming the poor water oxidation selectivity of WO_3, Pd nanoparticles (NPs) are deposited in a second AA-CVD step. Pd incorporation into WO_3 nanoneedle films has previously been achieved by AA-CVD, in both a single and two step synthesis.[15,16] However, to the best of our knowledge, the effect of Pd co-catalysts on WO_3 photoanodes applied to PEC water oxidation has not been previously studied. An additional annealing step, post Pd deposition, is undertaken to investigate the recognised effects of co-catalyst oxidation state on performance.[17] We identify PdO as a promising OEC for acidic conditions that enhances the water oxidation activity and selectivity of WO_3 towards oxygen evolution, to yield an impressive FE of 92%. Further investigations into the photoanodes, including the charge carrier properties using transient techniques, reveal the role of PdO in inducing favourable band bending and tuning oxygen vacancy concentrations in WO_3, to consequently improve electron transport through the nanoneedles.

2. Experimental

Materials synthesis

Nanostructured photoanodes were prepared by aerosol assisted chemical vapour deposition (AA-CVD).[14] FTO coated substrates were cleaned and heated in the reactor from the carbon block below. The inlet was fitted with a water-cooling jacket to prevent the decomposition of the precursors. During heating, deposition and cooling steps, the reactor was supplied with a steady flow of N_2 (3.5 L min^{-1}), regulated by a mass flow controller, with the exhaust from the reactor directed to the back of the fume hood. To obtain WO_3 nanoneedles, a precursor solution was prepared by dissolving $W(CO)_6$ (0.200 g) in a 2 : 1 mixture of acetone and methanol and sonicating for three minutes. The reactor was heated to 375 °C and the precursor solution was added in portions (8 × 5 mL). Aerosols were generated using an ultrasonic humidifier (2 MHz, Liquifog, Johnson Matthey) to generate a thick white aerosol that was carried into the reactor by the N_2 flow. Following deposition, the reactor and substrates were left to cool to room temperature. The as-synthesised blue films, WO_3(B), were annealed in a furnace at 500 °C for 12 hours to yield the white WO_3 films. $(NH_4)_2PdCl_4$ (0.003 g) was added to 50 mL methanol and sonicated for three minutes to obtain the precursor solution for Pd deposition. Pd nanoparticles were deposited onto annealed WO_3 to yield Pd/WO_3 using an analogous reactor set-up and method to above, except at 350 °C. Annealing at 500 °C for 12 hours post-Pd deposition was conducted on a portion of the films, with the resulting films labelled Pd(A)/WO_3.

Materials characterisation

A Leo Gemini 1525 Field Emission Gun scanning electron microscope (FEG SEM) was used for imaging the surface and cross-sectional morphology of the films, sputtered with a 10 nm Cr layer. Further imaging *via* high-resolution transmission electron microscopy (HR-TEM) was conducted with a Joel TEM 2100 Plus. X-ray diffraction (XRD) patterns were obtained with a Bruker D2 phaser with parallel beam optics equipped with a PSD LinxEye silicon strip detector, using Cu Kα radiation (40 kV and 40 mA). Raman spectra were collected with a Horiba LabRam Infinity spectrometer, with a HeNe laser (633 nm, 25 nW). The system was calibrated to a silicon reference and samples were analysed over the 150–1050 cm^{-1} range. Chemical analysis was performed by X-ray photoelectron spectroscopy (XPS) using a Thermo K-Alpha spectrometer with a monochromated Al Kα radiation source. Survey scans were carried out in the region of 0–1350 eV, at intervals of 0.1 eV and using a pass energy of 200 eV. Peaks were calibrated to the adventitious C 1s peak at 284.5 eV. CasaXPS software (Version 2.3.19PR1.0) was used for peak fitting and analysis.

The optical absorption of the photoanodes was characterised using a UV-Vis spectrometer (Shimadzu UV-2600) fitted with an integrating sphere. The absorbance (%A) was calculated from the measured diffuse reflectance (%R) and the transmittance (%T) using eqn (1):

$$\%A = 100 - (\%R + \%T) \quad (1)$$

The Kubelka–Munk transform was applied to the diffuse reflectance results to obtain a value approximately proportional to the absorption coefficient using eqn (2):

$$f(R) = \frac{(1-R)^2}{2R} = \frac{\alpha}{s} \quad (2)$$

where R is the measured diffuse reflectance of the sample, α is the absorption coefficient and s is the scattering coefficient. When using this approximation to obtain α, s is taken to be a constant independent of wavelength and the value of α. Estimations of the optical band gap were made from Tauc plots of $(\alpha h\nu)^{1/n}$ *vs.* $h\nu$, where the as calculated $f(R)$ was used in the place of α and the value of n is taken as 2, due to the indirect (allowed) band gap transition of WO_3.

This journal is © the Owner Societies 2021

Photoelectrochemical (PEC) measurements

PEC measurements were conducted in a homemade PEEK cell with a quartz window and a three-electrode set-up comprising of the as-synthesised photoanodes as the working electrode, Ag/AgCl/saturated KCl solution as the reference electrode (calibrated using Ferrocene as an internal reference) and a Pt mesh counter electrode. All electrodes were submerged into a 0.1 M H_2SO_4 (pH 1) electrolyte solution. Voltage was applied to the set-up using an Autolab potentiostat (PGSTAT 12). The incident photon to current efficiency (IPCE) was measured at 1.23 V_{RHE} and calculated at regular wavelength intervals from 250–800 nm, using a 75 W Xe arc lamp ($\sim$100 mW cm^{-2} white light intensity) fitted with a monochromator. Linear sweep voltammetry (LSV) measurements were taken in an anodic direction at a scan rate of 10 mV s^{-1} and under simulated 1 sun AM 1.5G irradiation. LSV sweeps were measured under light, dark and chopped-light conditions from 0.45–2.40 V_{RHE}. Stability tests were conducted using the same set-up as for the LSV measurements, but with the potential held at 1.23 V_{RHE} throughout.

The faradaic efficiency (FE) was measured using a H-cell, where the photoanode and reference electrode are in a separate chamber to the Pt counter electrode, with a frit between the chambers that allows ion exchange to occur. Otherwise, the set-up conditions were equivalent to the PEC measurements. Oxygen evolution from the photoanodes was detected in the gas phase, in the headspace above the electrolyte solution, by a Clark electrode (OXNP Unisense Oxygen Sensor) calibrated by the injection of known oxygen quantities. Similarly to LSV measurements, the photoanodes were illuminated with a 365 nm LED lamp mimicking the photon flux that would be absorbed at 1 sun irradiance.

The FE was calculated by dividing the measured O_2 by the theoretical O_2 evolution based on the photocurrent generation, using eqn (3):

$$\mathrm{FE}\ (\%) = \frac{\mathrm{O_2\ (mol)} \times N_\mathrm{A}}{\left(J_\mathrm{photo} \times A \times s \times \frac{1}{4}\right) \Big/ e} \times 100 \qquad (3)$$

where O_2 evolved is measured using the calibrated Clark electrode, J_{photo} is the integrated current measured over the illumination time and at a constant of applied potential of 1.23 V_{RHE}, A is the illuminated photoanode area, s is the measurement time period and e is the elementary charge constant. The multiplication by a quarter in the denominator is due to the consideration that four holes are required to evolve one mol of O_2 from water oxidation.

Theoretical solar photocurrent (TSP) calculation

The IPCE spectrum (measured at 1.23 V_{RHE}) was integrated and multiplied by AM 1.5G sunlight (100 mW cm^{-2}) to determine the theoretical solar photocurrent (TSP) using the following equation:

$$\mathrm{TSP}\ (\mathrm{mA\ cm^{-2}}) = \int_{E_\mathrm{bg}(\mathrm{nm})}^{280\mathrm{nm}} \mathrm{IPCE} \times \mathrm{AM\ 1.5G} \times 1000/1\mathrm{C}$$

where AM 1.5G is the solar photon flux (photons cm^{-2}), E_{bg} is the material bandgap ($\sim$490 nm) and 1C is 6.241 $\times$ 10^{18} electrons per second. The IPCE data was fit using a combined exponential decay and Gaussian model (with all fits showing $r^2 > 0.99$).

Transient photocurrent (TPC) measurements

TPC measurements were undertaken on photoanode samples in a PEC cell connected to a potentiostat, analogously to in the PEC measurements, under a constant potential as specified. Excitation of samples was conducted using the third harmonic output of a Nd:YAG laser (OPOTEK Inc, Opolette 355 II, 6 ns pulse width, λ_{ex} = 355 nm). A liquid light guide with a 0.5 cm diameter was used to direct the excitation pulse to the sample. Following excitation with the laser pulse, the transient photocurrent was obtained by measuring the voltage change with an oscilloscope (Tektronics DPO3012) from 10 μs to 0.1 s.

3. Results and discussion

The WO_3 films consist of a dense array of fine nanoneedles, up to 2 μm in length and $\sim$30–60 nm in width, as seen by SEM (Fig. 1). Considering the approximate electron (7 μm) and hole (150 nm) diffusion lengths in WO_3,[14] wherever electron–hole pairs are formed in the material, hole diffusion to the electrolyte interface and electron extraction from the photoanode can occur. Pd NPs were subsequently deposited onto the WO_3 films, also by the AA-CVD technique, to obtain Pd/WO_3 photoanodes, with those annealed post-Pd deposition termed Pd(A)/WO_3. HR-TEM images of Pd(A)/WO_3 show NPs of $\sim$4–10 nm in diameter, attributed to Pd by means of energy dispersive X-ray (EDX) analysis (Fig. S1, ESI†).

XRD patterns of all samples exhibit well defined peaks corresponding to crystalline monoclinic WO_3 and a dominant (002) peak due to preferential growth in this crystal plane (Fig. S2, ESI†),

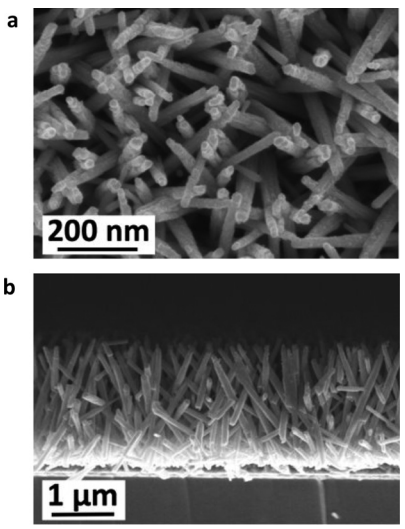


Fig. 1 (a) Top down, and (b) cross-sectional SEM images of WO_3, showing a maximum film thickness of 2 μm.

with the dominance of the (002) facet previously shown to increase reactivity and PEC performance.[18] This structure extends to photoanodes with Pd NPs, with no peaks corresponding to Pd species observed, likely due to the small quantity and nanoscale nature of the Pd-based material present. The crystal structure of the WO_3 coatings is confirmed by Raman spectroscopy (Fig. S3, ESI†), whereby the number and frequency of W–O–W stretching (718 cm^{-1} and 806 cm^{-1}) and O–W–O bending (272 cm^{-1} and 325 cm^{-1}) vibrations observed correspond to monoclinic WO_3.[19]

The surface chemical composition of the photoanodes was analysed by XPS and identified a near-complete oxidation of Pd to PdO, following the annealing treatment of Pd/WO_3 to Pd(A)/WO_3. The Pd 3d XPS spectrum of Pd/WO_3 (Fig. 2a) is dominated by a doublet, with $3d_{5/2}$ and $3d_{3/2}$ peaks at 335.6 eV and 340.9 eV respectively, corresponding to Pd metal.[20] The shoulder towards higher binding energies is fitted with two doublets of low intensity. The doublet with a $3d_{5/2}$ peak at 337.3 eV corresponds to the $3d_{5/2}$ peak of PdO.[20] Meanwhile, the second low intensity doublet with a $3d_{5/2}$ peak at 338.7 eV, is assigned to Pd^{2+} species in $PdCl_2$,[21] that arise from the incomplete decomposition of the Pd precursor ($(NH_4)_2PdCl_4$) during the AA-CVD synthesis. In contrast to Pd/WO_3, the dominant doublet in the Pd(A)/WO_3 spectrum (Fig. 2b) is assigned to PdO, with the $3d_{5/2}$ peak at 337.4 eV in good agreement with the low intensity PdO doublet observed prior to annealing. Although the Pd metal doublet is also observed here, it is of significantly lower intensity.

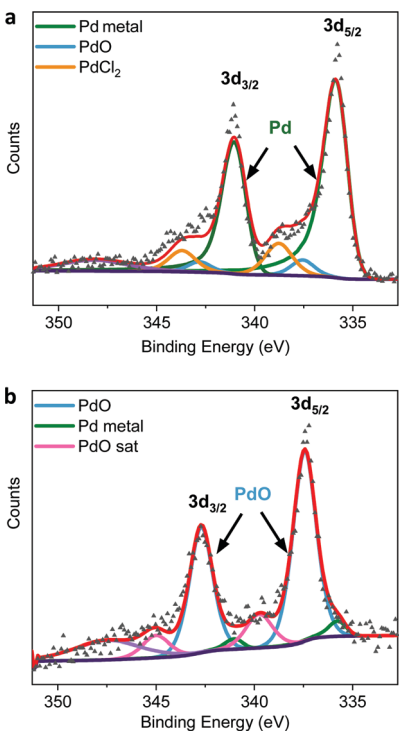


Fig. 2 Pd 3d XPS spectra for (a) Pd/WO_3 and (b) Pd(A)/WO_3. The red lines and grey triangles represent the summation of the fitted peaks and the raw data points respectively.

Oxygen vacancies in WO_3 induce sub-band gap defect states (V_O) that are situated below the conduction band.[22] It has been demonstrated that the concentration of V_O in WO_3 has profound effects on recombination rates and material properties, including visible light absorption and charge transport.[5,7,22–25] W^{5+} species neighbouring oxygen vacancy sites have a characteristic optical absorption extending into the near-IR.[22,24,25] This is demonstrated by the blue colour and intense near-IR absorption feature of V_O rich WO_3(B), compared to the white colour and diminished near-IR absorption of annealed WO_3 (Fig. S4, ESI†). Consequently, the decreased absorption intensity in the near-IR for Pd/WO_3 and Pd(A)/WO_3 indicates a further decrease in V_O concentration (Fig. S5, ESI†). The indirect band gap of ~2.8–2.9 eV estimated for our WO_3 using a Tauc plot (Fig. S6a, ESI†) does not differ significantly for Pd/WO_3 or Pd(A)/WO_3 (Fig. S6b and c, ESI†). The suppressed V_O concentration with Pd-based co-catalysts was semi-quantified (using the ratio of W^{5+} to W^{6+} peak areas in the XPS spectra, Table S1, ESI†) to reveal a near 25% decrease of V_O in WO_3 upon Pd addition in both Pd/WO_3 and Pd(A)/WO_3, coinciding with the change to the near-IR W^{5+} absorption. Given the known sensitivity of WO_3 properties to V_O,[24] this is significant and hence needs consideration when discussing the trends in performance between the photoanodes.

Following the characterisation of the as-synthesised materials, they were employed as photoanodes in a three-electrode set-up in 0.1 M H_2SO_4 to measure their PEC water oxidation performance. A comparison of the IPCE of the photoanodes at 1.23 V_{RHE} is displayed in Fig. 3a. The IPCE of WO_3-based photoanodes peaks at 325 nm and is notable up to 450 nm. The negligible IPCE at longer wavelengths demonstrates that the photocurrent is generated solely as a result of band gap excitation (with W^{5+} absorption at longer wavelengths unable to facilitate water oxidation). This is further corroborated by the negligible IPCE of WO_3(B) at all wavelengths despite the significant absorption by W^{5+}, due to insufficient tuning of

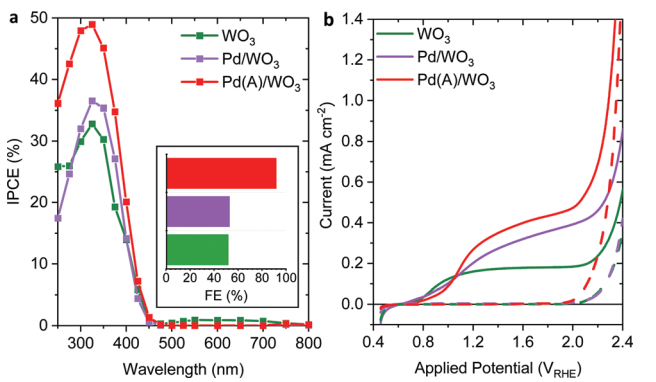


Fig. 3 PEC water oxidation performance of photoanodes under front illumination in 0.1 M H_2SO_4. (a) IPCE spectra measured at 1.23 V_{RHE} under 100 mW cm^{-2} white light. Inset of (a) shows the FE of the photoanodes at 1.23 V_{RHE}, irradiated with a 365 nm LED mimicking the photon flux that would be absorbed at 1 sun irradiance. (b) LSV measurements under light (solid line) and dark (dashed line) conditions, using simulated 1 sun AM 1.5G irradiation.

This journal is © the Owner Societies 2021

the V_O concentration.[7,22] The poor charge separation efficiency of the bare WO_3 upon light absorption is reflected by the low IPCE (33% at 325 nm). Hence, a co-catalyst that forms a junction and improves charge separation, or accelerates the rate of hole transfer from WO_3, is desirable to improve performance. Pd/WO_3 achieves a trivial IPCE increase over WO_3, however, Pd(A)/WO_3 results in an increase in IPCE to 49% at 325 nm. Given the analogous UV-Vis spectra of WO_3 and Pd(A)/WO_3 in the photoactive region (Fig. S5, ESI†), the IPCE increase is attributed to a decrease in recombination and/or improved catalysis, as opposed to a higher initial yield of photogenerated charges. The contact established between PdO NPs and WO_3 in Pd(A)/WO_3 is likely to resemble a p–n junction (given the n-type character of WO_3 and previous reports of PdO as a p-type material)[16,26,27] that improves charge separation by driving holes towards PdO and electrons in the opposite direction into bulk WO_3.

PEC properties of the photoanodes were further investigated by LSV measurements under simulated sunlight and dark conditions (Fig. 3b). The effect of illumination on the overall current is strong evidence of photocurrent generation after an onset potential of $\sim$0.55 V_{RHE} in all cases, similar to previous reports of WO_3 photoanodes.[7,14,28] The trend in photocurrent generation between samples at the standard water oxidation potential (1.23 V_{RHE}) correlates to that of the IPCE results, obtained at the same potential. The highest photocurrents at 1.23 V_{RHE} achieved by Pd(A)/WO_3 (0.28 mA cm^{-2}) are 75% greater than bare WO_3 (0.16 mA cm^{-2}), in agreement with the overall trends observed from the TSP calculations (Table S2, ESI†). The discrepancy from this trend at 0.8–1.0 V_{RHE} in the LSV measurements is ascribed to an energy barrier to charge transfer in Pd-decorated systems, which must be overcome to achieve the photocurrent enhancements. The rapid increase in current density at high applied potentials (in both light and dark conditions) is attributed to electrocatalytic water oxidation, the onset of which occurs earliest and most dramatically for Pd(A)/WO_3 and identifies the role of PdO in effectively enhancing the electrocatalytic water oxidation performance of WO_3. Over the 4 hour period of stability tests at 1.23 V_{RHE}, highly stable photocurrents were achieved by the photoanodes after a short initial stabilisation period (Fig. S7, ESI†), with only a 3.6% and 2.1% photocurrent decrease observed thereafter for WO_3 and Pd(A)/WO_3 respectively. Transient spikes in the chopped light LSV measurements are not observed for our systems (Fig. S8a, ESI†), in contrast to what is commonly observed for $BiVO_4$ and Fe_2O_3 photoanodes.[29,30] Such spikes are indicative of back electron–hole recombination of photogenerated charge pairs,[31–33] and their absence herein indicates that this recombination process is masked by sufficiently fast water oxidation kinetics, or that it occurs before the timescale of our measurements.

A comparison of the LSV traces under front and back illumination (Fig. S8b, ESI†) identifies electron extraction as the limiting charge carrier process in WO_3 (due to the preference for back illumination), in agreement with prior work.[7] In contrast, front illumination favours photocurrent generation in Pd(A)/WO_3 (however, it should be noted that back illumination of Pd(A)/WO_3 also remains more favourable than that of WO_3), indicating a switch to hole transport as the more limiting process, as discussed further later.

Now we turn to our comparison of the water oxidation efficiency of the photoanodes (Fig. 3a inset and Fig. S9, ESI†). WO_3 achieves a FE of 52%, in line with previous reports[14,28] and explained by the oxidation of SO_4^{2-} anions in the electrolyte to $S_2O_8^{2-}$ on the WO_3 surface.[8,9] Strikingly, Pd(A)/WO_3 achieves a greatly improved FE of 92% which confirms water oxidation as the origin of the higher photocurrents associated with this photoanode (little improvement is seen with Pd/WO_3) and highlights the role of PdO, or the PdO/WO_3 interface, in offering catalytic sites for improved water oxidation selectivity.

Alternative surface modification routes for improving the FE of WO_3 are compared with this work (Table S3, ESI†), to reveal that PdO addition is unique regarding the extent to which it improves FE without inhibiting photocurrent generation. For example, the addition of Cr_2O_3 nanocrystals[8] or a Al_2O_3 overlayer[34] results in modest improvements to the FE compared to PdO addition, with a reduction in photocurrent observed for the latter case. Meanwhile, the photoelectrochemical deposition of FeOOH significantly increases the FE (27% to 96% (entry 2)),[35] but also induces parasitic light absorption and inhibits photocurrent generation by 50% (whereas, PdO enhances photocurrent generation). Thus, amongst the surface modification routes explored to date, Pd(A)/WO_3 shows highly favourable properties for enhancing the FE and photocurrent.

Herein, we find consistent improvements in the IPCE, LSV and FE results when PdO co-catalysts are grown on WO_3 (Pd(A)/WO_3). As shown by XPS (Fig. 2), annealing results in a near-complete oxidation of metallic Pd^0 in Pd/WO_3, to Pd^{2+} (PdO) in Pd(A)/WO_3. Modelling of the band bending at the junction between WO_3 and the Pd NP species can help rationalise these differences (Fig. S10, ESI†).[36] We note that the models do not predict the band bending under operational conditions but do allow the distinct effects of PdO and Pd^0 at the surface to be compared. The junction between n-type WO_3 and p-type PdO NPs in Pd(A)/WO_3 results in band bending in WO_3 that facilitates hole transport to the surface and electron extraction *via* the back contact, whereas for Pd/WO_3 unfavourable band bending is observed. Moreover, the electric field present in PdO after equilibrium further drives holes away from WO_3 and towards the electrolyte junction, with no such driving force present with Pd^0. In addition to the contrasting effects on band bending in WO_3, the different oxidation states of Pd would result in different bonding and adsorption properties of oxygenated intermediates that drive water oxidation.[17,37]

The charge extraction characteristics of the photoanodes were assessed by TPC measurements, whereby the charge extracted was measured as a function of time following excitation by a laser pulse (Fig. 4). Pd(A)/WO_3 exhibits faster charge extraction rates than bare WO_3, whilst charge extraction in Pd/WO_3 is slower. The kinetics of electron extraction therefore support the band bending models (Fig. S10, ESI†), as compared to metallic Pd, the band bending that results with PdO favours

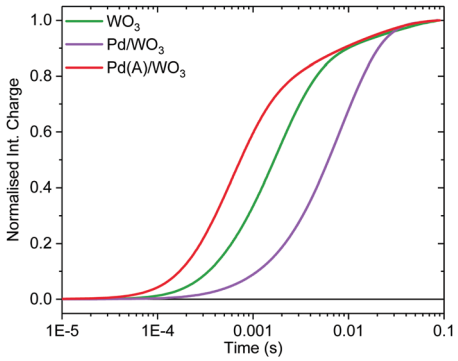


Fig. 4 A comparison of the charge extraction rates of the photoanodes following laser excitation (355 nm, 6 ns pulse width), held at 1.23 V_{RHE} in 0.1 M H_2SO_4.

electron extraction through the bulk WO_3. Our previous TPC studies on WO_3 nanoneedles showed that electron extraction through the bulk is hindered by an excess of oxygen vacancies.[7] Given that a decrease in V_O concentration is observed in both Pd(A)/WO_3 and Pd/WO_3 (Table S1 and Fig. S5, ESI†), but increased charge extraction rates are observed exclusively in the former, the V_O concentration cannot be the sole reason for this result. Therefore, the effects of the co-catalyst species on band bending are likely to dominate the charge extraction properties in this case.

With the difference in electron extraction properties between WO_3 and Pd(A)/WO_3 established, the rationale for their contrasting photocurrent generation behaviour under front and back illumination (Fig. S8b, ESI†) is twofold. Firstly, due to PdO deposition occurring predominantly on the top layer of the dense film, front illumination is required to generate holes that can diffuse to PdO sites and maximise the impact of the OEC. Secondly, the improved electron extraction properties of Pd(A)/WO_3, compared to WO_3, means that the advantages of generating holes in close proximity to PdO outweigh the benefits to electron extraction realised under back illumination.

4. Conclusions

In summary, nanostructured WO_3 photoanodes and Pd-based co-catalysts are synthesised *via* AA-CVD as a simple and up-scalable method. The PEC water oxidation performance of WO_3 is significantly enhanced by the addition of PdO as an OEC, with the promising stability of the photoanodes under acidic operating conditions maintained following this surface modification. We confirm the critical role of oxidising Pd species to achieve these performance enhancements, with negligible improvements observed with metallic Pd. Following the addition of the PdO co-catalyst, the FE of the photoanode surface is greatly improved from 52% to 92% for water oxidation, more greatly avoiding the deleterious side reactions that typically arise from the deep VBM of WO_3. Furthermore, PdO demonstrates beneficial effects on the photocurrent generation properties and increases the rate of charge extraction through the bulk of WO_3, likely due to the formation of a p–n junction.

Conflicts of interest

There are no conflicts to declare.

Acknowledgements

J. R. D. and L. F. thank the European Union's Horizon 2020 research and innovation programme (732840-A-LEAF). A. K. thanks the EPSRC for a Capital Award Emphasising Support for Early Career Researchers and the Royal Society for an Equipment Grant (RSG\R1\180434). Lee Tooley and Steve Atkins are thanked for constructing the chemical vapour deposition apparatus used in this work. S. C. thanks Imperial College for a Schrödinger Scholarship. A. A. W. thanks the EPSRC for a DTP studentship.

Notes and references

1 K. Sivula and R. Van De Krol, *Nat. Rev. Mater.*, 2016, **1**, 15010.
2 C. Jiang, S. J. A. Moniz, A. Wang, T. Zhang and J. Tang, *Chem. Soc. Rev.*, 2017, **46**, 4645–4660.
3 T. Jafari, E. Moharreri, A. S. Amin, R. Miao, W. Song and S. L. Suib, *Molecules*, 2016, **21**, 900.
4 X. Liu, F. Wang and Q. Wang, *Phys. Chem. Chem. Phys.*, 2012, **14**, 7894.
5 S. Liu, J. Gong, X. Chang, C. Li, A. Li, J. Zhang and T. Wang, *J. Mater. Chem. A*, 2017, **6**, 3350–3354.
6 P. Sharma, J. W. Jang and J. S. Lee, *ChemCatChem*, 2019, **11**, 157–179.
7 S. Corby, L. Francàs, S. Selim, M. Sachs, C. Blackman, A. Kafizas and J. R. Durrant, *J. Am. Chem. Soc.*, 2018, **140**, 16168–16177.
8 Z. Hu, M. Xu, Z. Shen and J. C. Yu, *J. Mater. Chem. A*, 2015, **3**, 14046–14053.
9 J. A. Seabold and K. S. Choi, *Chem. Mater.*, 2011, **23**, 1105–1112.
10 Q. Mi, A. Zhanaidarova, B. S. Brunschwig, H. B. Gray and N. S. Lewis, *Energy Environ. Sci.*, 2012, **5**, 5694–5700.
11 J. H. Kim, J. W. Jang, H. J. Kang, G. Magesh, J. Y. Kim, J. H. Kim, J. Lee and J. S. Lee, *J. Catal.*, 2014, **317**, 126–134.
12 K. S. Joya, M. A. Ehsan, N. U. A. Babar, M. Sohail and Z. H. Yamani, *J. Mater. Chem. A*, 2019, **7**, 9137–9144.
13 M. Ling and C. Blackman, *Phys. Status Solidi C*, 2015, **12**, 869–877.
14 A. Kafizas, L. Francàs, C. Sotelo-Vazquez, M. Ling, Y. Li, E. Glover, L. McCafferty, C. Blackman, J. Darr and I. Parkin, *J. Phys. Chem. C*, 2017, **121**, 5983–5993.
15 F. E. Annanouch, Z. Haddi, M. Ling, F. Di Maggio, S. Vallejos, T. Vilic, Y. Zhu, T. Shujah, P. Umek, C. Bittencourt, C. Blackman and E. Llobet, *ACS Appl. Mater. Interfaces*, 2016, **8**, 10413–10421.

 This journal is © the Owner Societies 2021

16 F. E. Annanouch, S. Roso, Z. Haddi, S. Vallejos, P. Umek, C. Bittencourt, C. Blackman, T. Vilic and E. Llobet, *Thin Solid Films*, 2016, **618**, 238–245.
17 H. He, J. Chen, D. Zhang, F. Li, X. Chen, Y. Chen, L. Bian, Q. Wang, P. Duan, Z. Wen and X. Lv, *ACS Catal.*, 2018, **8**, 6617–6626.
18 S. Wang, H. Chen, G. Gao, T. Butburee, M. Lyu, S. Thaweesak, J. H. Yun, A. Du, G. Liu and L. Wang, *Nano Energy*, 2016, **24**, 94–102.
19 T. Siciliano, A. Tepore, G. Micocci, A. Serra, D. Manno and E. Filippo, *Sens. Actuators, B*, 2008, **133**, 321–326.
20 T. Pillo, R. Zimmermann, P. Steiner and S. Hüfner, *J. Phys.: Condens. Matter*, 1997, **9**, 3987–3999.
21 M. C. Militello and S. J. Simko, *Surf. Sci. Spectra*, 1994, **3**, 402–409.
22 M. Sachs, J. S. Park, E. Pastor, A. Kafizas, A. A. Wilson, L. Francàs, S. Gul, M. Ling, C. Blackman, J. Yano, A. Walsh and J. R. Durrant, *Chem. Sci.*, 2019, **10**, 5667–5677.
23 S. K. Deb, *Sol. Energy Mater. Sol. Cells*, 2008, **92**, 245–258.
24 S. Corby, L. Francás, A. Kafizas and J. Durrant, *Chem. Sci.*, 2020, **11**(11), 2907–2914, DOI: 10.1039/C9SC06325K.
25 S. Corby, E. Pastor, Y. Dong, X. Zheng, L. Francàs, M. Sachs, S. Selim, A. Kafizas, A. A. Bakulin and J. R. Durrant, *J. Phys. Chem. Lett.*, 2019, **10**, 5395–5401.
26 D. B. Rogers, R. D. Shannon and J. L. Gillson, *J. Solid State Chem.*, 1971, **3**, 314–316.
27 H. Okamoto and T. Asô, *Jpn. J. Appl. Phys., Part 1*, 1967, **6**, 779.
28 C. Fàbrega, S. Murcia-López, D. Monllor-Satoca, J. D. Prades, M. D. Hernández-Alonso, G. Penelas, J. R. Morante and T. Andreu, *Appl. Catal., B*, 2016, **189**, 133–140.
29 Y. Ma, A. Kafizas, S. R. Pendlebury, F. Le Formal and J. R. Durrant, *Adv. Funct. Mater.*, 2016, **26**, 4951–4960.
30 P. Tang, L. Han, F. S. Hegner, P. Paciok, M. Biset-Peiró, H. Du, X. Wei, L. Jin, H. Xie, Q. Shi, T. Andreu, M. Lira-Cantú, M. Heggen, R. E. Dunin-Borkowski, N. López, J. R. Galán-Mascarós, J. R. Morante and J. Arbiol, *Adv. Energy Mater.*, 2019, 1901836.
31 Y. Ma, S. R. Pendlebury, A. Reynal, F. Le Formal and J. R. Durrant, *Chem. Sci.*, 2014, **5**, 2964–2973.
32 Y. Ma, F. Le Formal, A. Kafizas, S. R. Pendlebury and J. R. Durrant, *J. Mater. Chem. A*, 2015, **3**, 20649–20657.
33 R. Godin, A. Kafizas and J. R. Durrant, *Curr. Opin. Electrochem.*, 2017, **2**, 136–143.
34 W. Kim, T. Tachikawa, D. Monllor-Satoca, H. Il Kim, T. Majima and W. Choi, *Energy Environ. Sci.*, 2013, **6**, 3732–3739.
35 C. R. Lhermitte, J. Garret Verwer and B. M. Bartlett, *J. Mater. Chem. A*, 2016, **4**, 2960–2968.
36 R. Varache, C. Leendertz, M. E. Gueunier-Farret, J. Haschke, D. Muñoz and L. Korte, *Sol. Energy Mater. Sol. Cells*, 2015, **141**, 14–23.
37 I. Katsounaros, S. Cherevko, A. R. Zeradjanin and K. J. J. Mayrhofer, *Angew. Chem., Int. Ed.*, 2014, **53**, 102–121.